

Analytical model and dynamical phase-field simulation of terahertz transmission across ferroelectrics

Taorui Chen¹, Bo Wang³, Yujie Zhu¹, Shihao Zhuang¹, Long-Qing Chen², Jia-Mian Hu^{1*}

¹*Department of Materials Science and Engineering, University of Wisconsin-Madison, Madison, WI, 53706, USA*

²*Department of Materials Science and Engineering, The Pennsylvania State University, University Park, Pennsylvania, 16802, USA*

³*Materials Science Division, Lawrence Livermore National Laboratory, Livermore, CA 94550, USA*

Abstract

We theoretically investigate the steady-state transmission of continuous terahertz (THz) wave across a freestanding ferroelectric slab. Based on the Landau-Ginzburg-Devonshire theory of ferroelectrics and the coupled equations of motion for polarization and electromagnetic (EM) waves, we derive the analytical expressions of the frequency- and thickness-dependent dielectric susceptibility and transmission coefficient at the thin slab limit in the harmonic excitation regime. When the slab thickness is much smaller than the THz wavelength in the ferroelectric, the analytical predictions agree well with the numerical simulations from a dynamical phase-field model that incorporates the coupled dynamics of strain, polarization, and EM wave in multiphase systems. At larger thicknesses, the transmission is mainly determined by the frequency-dependent attenuation of THz waves in the ferroelectric and the formation of a standing polarization/THz wave. Our results advance the understanding of the interaction between THz wave and ferroelectrics and suggest the potential of exploiting ferroelectrics to achieve low-heat-dissipation, nonvolatile voltage modulation of THz transmission for high-data-rate wireless communication.

*E-mail: jhu238@wisc.edu

I. Introduction

The increasing demand for higher-data-rate wireless communication has been driving the efforts of exploiting the abundant frequency resources in the terahertz (THz) band (frequency: 0.1-10 THz) [1,2]. To realize THz communication, the ability to modulate both the amplitude and phase of a propagating THz wave via a gate voltage is crucial. Conventional approach involves the use of semiconductors, where the application of a voltage allows tuning the local carrier concentration and hence the local conductivity and permittivity. As a result, both the amplitude [3–8] and phase [9–11] modulation can be achieved. An alternative approach is to use ferroelectric materials, which contain electric-field switchable spontaneous polarization \mathbf{P} . In archetypal ferroelectrics such as BaTiO_3 and PbTiO_3 , the appearance of \mathbf{P} is attributed to the condensation of a soft mode phonon below the Curie temperature. In these materials, the resonance frequency of \mathbf{P} (soft mode phonon) is in the THz regime [12] and can be tuned by electric field, temperature, strain, etc [13]. Therefore, \mathbf{P} can resonantly interact with the incident THz wave, leading to a large polarization current $\partial\mathbf{P}/\partial t$ that in turn produces strong THz radiation. The radiated THz wave will then be superimposed with the incident THz wave, leading to an amplitude and phase modulation. Compared to semiconductors, the ferroelectrics-based approach can enable a lower-heat-dissipation and nonvolatile voltage modulation, which are both critical to on-chip thermal management.

The transmission of THz wave in ferroelectrics is critically determined by the dynamical response of \mathbf{P} to a THz electric field. Experimentally, time-resolved THz transmission spectroscopy has been used to measure the frequency-dependent complex dielectric permittivity of ferroelectrics in the THz band [14–21]. Contribution of different lattice modes to the permittivity can be analyzed by a classical damped oscillator dispersion model, through which key parameters such as resonant frequencies and damping coefficients can be evaluated. More recently, THz pump ultrafast x-ray diffraction has been used to directly probe the lattice/polarization dynamics inside a ferroelectric material [22–24]. Computationally, both the molecular dynamics [25–28] and the mesoscale dynamical phase-field simulations [13,24] have been used to understand and predict the THz-field-driven polarization dynamics in ferroelectrics. However, to our knowledge, there have been almost no theoretical and computational studies on the transmission of THz wave across a ferroelectric material. In this article, we analytically and numerically predict frequency-dependent THz wave transmission in a freestanding ferroelectric BaTiO_3 slab varying from a few nanometers to tens of micrometers. Spatiotemporal evolution of the coupled polarization vector \mathbf{P} and a THz wave in the ferroelectric is obtained using phase-field simulations.

Specifically, we consider a small-amplitude incident continuous THz wave to drive the polarization oscillation within the harmonic regime. Based on the Landau-Ginzburg-Devonshire (LGD) theory of ferroelectrics and the coupled equation of motions for the \mathbf{P} and electromagnetic (EM) wave, we develop an analytical model for predicting the frequency- and thickness- dependent THz dielectric susceptibility and THz wave transmission in ferroelectrics in the regime of steady-state harmonic excitation at the thin slab limit (i.e., the slab thickness is much smaller than the THz wavelength in the slab). When the ferroelectric slab is sufficiently thin, the analytical predictions agree well with numerical simulation results obtained from a dynamical phase-field model that incorporates fully coupled dynamics of polarization, strain, and EM waves [13]. At relatively large thicknesses, it is found that the formation of standing polarization wave can lead to oscillatory thickness dependences on the THz wave transmission coefficient. Our results advance our understanding of the THz wave-matter interaction in ferroelectrics. The dynamical phase-field model is also applicable to systems with inhomogeneous polarization configurations and can therefore be used to guide the design of ferroelectrics-based active THz wave modulators for high-data-rate wireless communication applications.

II. Analytical model of THz dielectric and transmission spectra in single-domain ferroelectrics

Let us consider the normal incidence of a single-frequency, continuous sinusoidal THz plane wave transmitting through a finite-thickness ferroelectric slab along its z axis, as shown in Fig. 1(a). At the initial equilibrium state, the ferroelectric slab has a spatially uniform spontaneous polarization along $+x$. The incident THz wave in the air can be written as $E_i^{\text{inc}}(z, t) = E_i^{0,\text{inc}} e^{i(k_a z - \omega t)}$, $i = x, y, z$, where $E_i^{0,\text{inc}}$ is the amplitude of the electric-field component; k_a and ω are the angular wavenumber and angular frequency in the air, respectively. The transmission coefficient T (reflection coefficient R) is calculated as the intensity of the transmitted THz wave at the surface plane A_2 (reflected THz wave at the surface plane A_1) divided by the intensity of the incident THz wave. Mathematically,

$$T = \frac{\frac{1}{2} c \kappa_0 \sum_i (E_i^{0,A_2})^2}{\frac{1}{2} c \kappa_0 \sum_i (E_i^{0,\text{inc}})^2} = \frac{\sum_i (E_i^{0,A_2})^2}{\sum_i (E_i^{0,\text{inc}})^2}; \quad R = \frac{\frac{1}{2} c \kappa_0 \sum_i (E_i^{0,A_1})^2}{\frac{1}{2} c \kappa_0 \sum_i (E_i^{0,\text{inc}})^2} = \frac{\sum_i (E_i^{0,A_1})^2}{\sum_i (E_i^{0,\text{inc}})^2}, \quad i = x, y, z, \quad (1)$$

where c is the speed of light in the vacuum; κ_0 is the vacuum permittivity; E_i^{0,A_2} and E_i^{0,A_1} are the amplitudes of the electric-field component of the transmitted THz wave at the plane A_2 and plane A_1 , respectively. In the thin slab limit, it is rational to omit the reflection and refraction of the incident THz wave at the two ferroelectric/air interfaces and wave interference [29]. In this case, E_i^{0,A_2} is a superposition of the incident and radiated THz wave, yet E_i^{0,A_1} is contributed purely by the radiated THz wave. Since the amplitude of the incident THz wave $E_i^{0,\text{inc}}$ is known, the key is to calculate the E_i^{rad} , the radiated wave generated by the oscillating polarization in the ferroelectric.

The plane-wave solution of E_i^{rad} can be derived by assuming a zero out-of-plane polarization component in the ferroelectric (i.e., $P_z=0$, which is valid when E_z^{inc} is zero). In the thin slab limit, the oscillating polarization is spatially uniform (in-phase) along the z axis. The radiation electric field is also homogeneous across the slab, and can be calculated as (details are in Supplemental Material [30]),

$$E_i^{\text{rad},A_1}(t) = E_i^{\text{rad},A_2}(t) = E_i^{\text{rad}}(t) = -\frac{1}{2} \frac{d}{\kappa_0 c} \frac{\partial P_i(t)}{\partial t}, \quad i = x, y. \quad (2)$$

When the ferroelectric is excited by a small-amplitude THz wave with an angular frequency ω , nonlinear effect such as second harmonic generation can be neglected. As a result, the steady-state harmonic oscillation of the local polarization in the ferroelectric can be described by $P_i(t) = P_i^{\text{eq}} + \Delta P_i(t) = P_i^{\text{eq}} + \Delta P_i^0 e^{i(-\omega t + \varphi)}$, where ΔP_i^0 and φ are the amplitude and phase difference (with respect to the incident THz wave) of the polarization oscillation, respectively; P_i^{eq} is the spontaneous polarization value at the initial equilibrium state. Since P_i^{eq} can be obtained by minimizing the LGD potential of the ferroelectric, the key is to analytically calculate the frequency-dependent ΔP_i^0 and φ of the harmonic polarization oscillation.

To derive the formulae of ΔP_i^0 and φ in the regime of harmonic polarization oscillation, we first rewrite the equation of motion for polarization [31–34] into the following harmonic form,

$$\mu \frac{\partial^2 \Delta P_i}{\partial t^2} + \gamma_i \frac{\partial \Delta P_i}{\partial t} = E_i^{\text{inc},0} e^{-i\omega t} - \omega_i^2 \mu \Delta P_i + E_i^{\text{rad}}, \quad i = x, y, \quad (3)$$

where $\mu = (\kappa_0 \omega_p^2)^{-1}$ is the mass coefficient (polarization inertia) and $\omega_p = \sqrt{\frac{1}{\kappa_0 V_0} \sum_n \frac{Q_n^2}{M_n}}$ is the plasma frequency, where Q_n and M_n are the charge and mass of the n th charged ion in a unit cell with volume

V_0 [34]; γ_i is the phenomenological damping coefficient that can be related to crystal viscosity of the ferroelectric [35]. The first term on the right of Eq. (3) assumes that the local electric fields from the incident THz wave in the ferroelectric slab are spatially uniform and in-phase, which is valid in the thin slab limit. The second term on the right of Eq. (3) describes the effective electric field arising from the Landau energy density and elastic energy density in the harmonic regime, where the resonant frequency of the polarization oscillation ω_i can be written as,

$$\omega_i = \sqrt{-\frac{A_i + B_i}{\mu}}; A_i = \left. \frac{\partial E_i^{\text{Landau}}}{\partial P_i} \right|_{P=P_i^{\text{eq}}}; B_i = \left. \frac{\partial E_i^{\text{Elas}}}{\partial P_i} \right|_{P=P_i^{\text{eq}}}. \quad (4)$$

Since the effective electric field $E_i^{\text{Landau}} = -\left. \frac{\partial f^{\text{Landau}}}{\partial P_i} \right|_{P=P_i^{\text{eq}}}$ and $E_i^{\text{Elas}} = -\left. \frac{\partial f^{\text{Elas}}}{\partial P_i} \right|_{P=P_i^{\text{eq}}}$, the coefficients

A_i and B_i are essentially the local curvature of the Landau and elastic energy density at their respective minimum point. Detailed mathematical expressions of A_i and B_i are provided in Supplemental Material [30]. Plugging in the E_i^{rad} in Eq. (3) into Eq. (4), one has,

$$\mu \frac{\partial^2 \Delta P_i}{\partial t^2} + \gamma_i^{\text{eff}} \frac{\partial \Delta P_i}{\partial t} = -\omega_i^2 \mu \Delta P_i + E_i^{\text{inc},0} e^{-i\omega t} \quad i = x, y, \quad (5)$$

where the effective damping coefficient $\gamma_i^{\text{eff}} = \gamma_i + \frac{1}{2} \frac{d}{k_0 c}$. Equation (5) indicates the radiation electric field acts as an additional source for the damping term that governs the relaxation of polarization dynamics. Substituting the steady-state solution $\Delta P_i(t) = \Delta P_i^0 e^{i(-\omega t + \varphi)}$ into Eq. (5) yields the following relation,

$$\Delta P_i(\omega) = \chi_{ii}(\omega) E_i^0 e^{-i\omega t} = \frac{E_i^0 e^{-i\omega t}}{\mu(\omega_i^2 - \omega^2) - \gamma_i^{\text{eff}} i\omega}, \quad (6)$$

where $\chi_{ii}(\omega)$ is the diagonal component of the frequency-dependent dielectric susceptibility. Its real and imaginary component can be obtained as,

$$\chi_{ii}^{\text{Re}}(\omega) = \frac{\mu(\omega_i^2 - \omega^2)}{\mu^2(\omega_i^2 - \omega^2)^2 + (\gamma_i^{\text{eff}})^2 \omega^2}; \chi_{ii}^{\text{Im}}(\omega) = \frac{\gamma_i^{\text{eff}} \omega}{\mu^2(\omega_i^2 - \omega^2)^2 + (\gamma_i^{\text{eff}})^2 \omega^2}. \quad (7)$$

The non-diagonal components of the dielectric susceptibility χ_{ij} ($i \neq j$) would be zero under the assumption of harmonic oscillation for the polarization. The total dielectric permittivity $\kappa_{ii}(\omega) = \kappa_{ii}^{\text{Re}}(\omega) + i\kappa_{ii}^{\text{Im}}(\omega)$, where the real component of the dielectric permittivity is $\kappa_{ii}^{\text{Re}}(\omega) = \kappa_b + \frac{\chi_{ii}^{\text{Re}}(\omega)}{\kappa_0}$ while the imaginary dielectric permittivity is $\kappa_{ii}^{\text{Im}}(\omega) = \frac{\chi_{ii}^{\text{Im}}(\omega)}{\kappa_0}$. Here κ_b is the background dielectric permittivity of ferroelectrics, which is related to the electronic polarization and other non-permanent ionic polarization induced by the local electric field [36–38]. Under THz or lower frequency excitation where the (ferroelectric) polarization \mathbf{P} can follow the applied electric field \mathbf{E} , the anisotropy in the response of the dielectric displacement \mathbf{D} to \mathbf{E} is mainly determined by \mathbf{P} . In this regard, κ_b is typically considered to be isotropic and frequency independent. From Eq. (6), we can also derive,

$$\Delta P_i^0(\omega) = \text{sgn}\left(\frac{\sin \varphi}{\gamma_i^{\text{eff}}}\right) E_i^0 \sqrt{\frac{1}{(\omega_i^2 \mu - \mu \omega^2)^2 + (\gamma_i^{\text{eff}} \omega)^2}} \quad (8a)$$

$$\varphi(\omega) = \text{atan} \left[\frac{\gamma_i^{\text{eff}} \omega}{\mu(\omega_i^2 - \omega^2)} \right], \text{ when } \omega < \omega_i; \varphi(\omega) = \text{atan} \left[\frac{\gamma_i^{\text{eff}} \omega}{\mu(\omega_i^2 - \omega^2)} \right] + \pi, \text{ when } \omega > \omega_i \quad (8b)$$

Now consider the normal incidence of a continuous THz wave with an electric-field component along the x axis ($E_x^{\text{inc}} \neq 0$, $E_y^{\text{inc}} = E_z^{\text{inc}} = 0$) as an example. In this case, only the P_x will oscillate, hence the radiation electric field E_i^{rad} only has the x -component. Thus, the electric field at the plane A_2 can be expressed as,

$$E_x^{A_2} = E_x^{0,\text{inc}} e^{-i\omega t} + \frac{1}{2} \frac{d}{\kappa_0 c} i \omega \Delta P_x^0 e^{i(-\omega t + \varphi)}. \quad (9)$$

The temporal waveform of $E_x^{A_2}(t)$ is the real component of the complex function in Eq. (9), i.e.,

$$E_x^{A_2}(t) = E_x^{0,\text{inc}} \cos(\omega t) + \frac{1}{2} \frac{d}{\kappa_0 c} \omega \Delta P_x^0 \sin(\omega t - \varphi). \quad (10)$$

Since both $E_x^{0,\text{inc}}$ and ω are the inputs, and the analytical solutions of ΔP_x^0 and φ are provided in Eqs. (8a-b), one can analytically predict the entire temporal waveform and therefore the amplitude E_x^{0,A_2} . Accordingly, the transmission coefficient can be calculated by $T = (E_x^{0,A_2}/E_x^{0,\text{inc}})^2$. The reflection coefficient can be calculated as $R = (E_x^{0,A_1}/E_x^{0,\text{inc}})^2$. The electric field at the plane A_1 is the same as the radiation field shown in Eq. (2), and thus the amplitude E_x^{0,A_1} can be analytically calculated. We note that $T + R < 1$ because the damping of polarization wave (via the γ_i in Eq. (3)) leads to THz wave absorption.

III. Dynamical phase-field simulations

In this section we present our dynamical phase-field model which allow numerical simulation of THz transmission, reflection, and absorption in ferroelectrics with spatially inhomogeneous polarization. The propagation of THz wave is coupled to both polarization dynamics and strain dynamics in a ferroelectric system. Therefore, the simulation of THz wave transmission requires solving the coupled equations of motion for EM waves, polarization \mathbf{P} , and the mechanical displacement \mathbf{u} . Rearranging the Maxwell's equations (see Supplemental Material [30]), one has,

$$\frac{\partial \mathbf{E}}{\partial t} = \frac{1}{\kappa_0 \kappa_b} \left(\nabla \times \mathbf{H} - \mathbf{J}^f - \frac{\partial \mathbf{P}}{\partial t} \right), \quad (11)$$

$$\frac{\partial \mathbf{H}}{\partial t} = -\frac{1}{\mu_0} (\nabla \times \mathbf{E}). \quad (12)$$

It is noteworthy that Eqs. (11-12) are solved for the entire system shows in Fig. 1(a), which includes both the ferroelectric phase and the air phase. As indicated by Eq. (11), the electric-field component of the EM wave (\mathbf{E}) is related to both the free electric current \mathbf{J}^f and the polarization current $\partial \mathbf{P} / \partial t$. We set the background dielectric permittivity $\kappa_b = 5$ [39] in the ferroelectric BaTiO₃, and $\kappa_b = 1$ in the air. The evolution of the polarization \mathbf{P} is governed by,

$$\mu \frac{\partial^2 P_i}{\partial t^2} + \gamma_i \frac{\partial P_i}{\partial t} = E_i^{\text{eff}}, \quad (13)$$

where the total effective electric field $E_i^{\text{eff}} = E_i^{\text{Landau}} + E_i^{\text{Elas}} + E_i^{\text{Grad}} + E_i^{\text{d}} + E_i^{\text{ext}}$ include effective electric fields arising (E_i^{Landau} and E_i^{Elas}) from the Landau free energy and elastic energy densities, the field from the gradient energy density E_i^{Grad} , the depolarization field E_i^{d} , and the externally applied electric

field E_i^{ext} . The expression of E_i^{Landau} (available in [13]) is a seventh-order polynomial of the polarization P_i , and thus Eq. (13) would describe an anharmonic polarization oscillation if the amplitude of ΔP_i is large enough. The $E_i^{\text{Elas}} = -\frac{\partial f^{\text{Elas}}}{\partial P_i}$ is given as,

$$E_i^{\text{Elas}} = 2[q_{11}(\varepsilon_{ii} - \varepsilon_{ii}^0) + q_{12}(\varepsilon_{jj} + \varepsilon_{kk} - \varepsilon_{jj}^0 - \varepsilon_{kk}^0)]P_i + 2q_{44}[(\varepsilon_{ij} - \varepsilon_{ij}^0)P_j + (\varepsilon_{ik} - \varepsilon_{ik}^0)P_k], \quad (14)$$

where $q_{11} = c_{11}Q_{11} + 2c_{12}Q_{12}$, $q_{12} = c_{11}Q_{12} + c_{12}(Q_{11} + Q_{12})$, and $q_{44} = 2c_{44}Q_{44}$; the stress-free strain $\varepsilon_{ii}^0 = Q_{11}P_i^2 + Q_{12}(P_j^2 + P_k^2)$ and $\varepsilon_{ij}^0 = Q_{44}P_iP_j$, with $i = x, y, z$, and $j \neq i, k \neq i, j$. Q_{11} , Q_{12} , and Q_{44} are the electrostrictive coefficients of the ferroelectric; c_{11} , c_{12} , and c_{44} are the elastic stiffness coefficients of the ferroelectric. The total strain $\boldsymbol{\varepsilon}$ can be written as $\boldsymbol{\varepsilon} = \boldsymbol{\varepsilon}^{\text{eq}} + \Delta\boldsymbol{\varepsilon}$. $\boldsymbol{\varepsilon}^{\text{eq}}$ is the total strain at the initial equilibrium state, which describes the macroscopic shape change of the ferroelectric and can be obtained by solving the mechanical equilibrium equation $\nabla \cdot \boldsymbol{\sigma}^{\text{eq}} = 0$. Here $\boldsymbol{\sigma}^{\text{eq}}$ is the stress distribution at the initial equilibrium state. For stress-free ferroelectric layer, $\boldsymbol{\varepsilon}^{\text{eq}} = \boldsymbol{\varepsilon}^{0, \text{eq}}$. The dynamical strain $\Delta\boldsymbol{\varepsilon}$, which originates from the oscillating polarization, can be obtained by numerically solving the elastodynamic equation,

$$\rho \frac{\partial^2 \Delta \mathbf{u}}{\partial t^2} = \nabla \cdot \left(\Delta \boldsymbol{\sigma} + \beta \frac{\partial \Delta \boldsymbol{\sigma}}{\partial t} \right). \quad (15)$$

Here ρ is the mass density and β is the stiffness damping coefficient. $\Delta \mathbf{u} = \mathbf{u} - \mathbf{u}^{\text{eq}}$ is the dynamical displacement and $\Delta \boldsymbol{\sigma} = \boldsymbol{\sigma} - \boldsymbol{\sigma}^{\text{eq}}$ is the dynamical stress. One can also write $\Delta \sigma_{ij} = c_{ijkl}(\Delta \varepsilon_{kl} - \Delta \varepsilon_{kl}^0)$, with $\Delta \varepsilon_{kl}^0 = \varepsilon_{kl}^0 - \varepsilon_{kl}^{0, \text{eq}}$ and $\Delta \varepsilon_{kl} = \frac{1}{2} \left(\frac{\partial \Delta u_k}{\partial l} + \frac{\partial \Delta u_l}{\partial k} \right)$. $E_i^{\text{Grad}} = -\frac{\delta f^{\text{grad}}}{\delta P_i} = G \nabla^2 P_i$, where G is the isotropic gradient energy coefficient. E_i^{ext} is the same as the electric-field component of the propagating EM wave in the system, which is obtained by averaging the simulated E_i staggered on the edges of the Yee lattice. E_i^{d} can be expressed as $E_i^{\text{d}}(t) = E_i^{\text{d,eq}} + \Delta E_i^{\text{d}}(t)$. The depolarization field at the initial equilibrium state ($t=0$), $E_i^{\text{d,eq}}$, can be obtained by solving the electrostatic equilibrium equation $\nabla \cdot (\kappa_0 \kappa_b E_i^{\text{d,eq}} + P_i^{\text{eq}}) = 0$. For a 1D system which has periodic boundary condition within the xy plane, one has $(E_x^{\text{d,eq}}, E_y^{\text{d,eq}}, E_z^{\text{d,eq}}) = (0, 0, -\frac{P_z^{\text{eq}}}{\kappa_0 \kappa_b})$. The dynamically changing depolarization field ΔE_i^{d} , which emerges when \mathbf{P} starts to evolve, does not need to be calculated separately. Rather, the $E_i(t)$ obtained by numerically solving Eqs. (11) and (12) via the finite-difference time-domain (FDTD) solver on a Yee lattice can automatically satisfy the continuity equation for electric displacement, i.e., $\nabla \cdot D_i = \nabla \cdot (\kappa_0 \kappa_b E_i + P_i) = 0$. The stress-free mechanical boundary condition at the top and bottom surfaces of the ferroelectric layer is automatically satisfied after setting the elastic stiffness coefficient $c_{ijkl} \approx 0$ for the air phase.

The entire system is discretized into one-dimensional (1D) cells of $1 \times 1 \times \Delta z N$ with a cell size $\Delta z = 1$ nm. The bottom 40 cells (40 nm) and the top 20 cells (20 nm) are the air phase, where $\rho \approx 0$, $\beta \approx 0$, $c_{ijkl} \approx 0$. The remaining cells are designated the ferroelectric BaTiO₃. The free electric current source is injected at the coordinate $z = -20$. Materials parameters used for BaTiO₃ are the same as those in [13]. The Neumann type boundary condition $\partial P_i / \partial z = 0$ ($i = x, y, z$) is used when solving Eq. (13), which assumes a full compensation of polarization charge at the surfaces [40] and would lead to the reflection of polarization wave at the two surfaces of the ferroelectric slab. Conventional Yee lattice is used to discretize the EM wave and FDTD is used to solve Eqs. (12, 13), during which the absorbing boundary condition, $\frac{\partial \mathbf{E}}{\partial z} = -\frac{1}{c} \frac{\partial \mathbf{E}}{\partial t}$, is applied to the topmost and bottommost cell of the entire computational system. Due to the use of the staggered grids for \mathbf{E} and \mathbf{H} in the Yee lattice (see Fig. 1(b)), the actual thickness of the BaTiO₃ layer considered in numerical simulations would be $(N-60+1)\Delta z$, where the additional grid results from the two

half grids at the interfaces. Central finite difference is used for calculating spatial derivatives. All dynamical equations are solved simultaneously using the classical Runge-Kutta method for time-marching with a real-time step $\Delta t = 2 \times 10^{-18}$ s. The high numerical accuracy of our FDTD solver is demonstrated by simulating the EM wave transmission across a freestanding dielectric layer with spontaneous polarization $\mathbf{P}=0$ and comparing the simulation results with analytical solution derived from the #SHAARP package [41] (see Supplemental Material [30]). To evaluate the transmission coefficient from the numerical simulations, we first obtain the $E_i^{0,\text{inc}}$ by a control simulation with $\mathbf{P}=0$ and $\kappa_b = 1$, and then record the E_i^{0,A_2} at the plane A_2 after the polarization oscillation reaches the steady-state regime. The transmission coefficient can then be evaluated via Eq. (1). The radiation electric field $E_i^{\text{rad}}(z,t)$ can be approximated by subtracting the simulated $E_i^{\text{inc}}(z,t)$ in the control simulation from the total $E_i(z,t)$.

IV. Results and Discussion

To generate a continuous incident THz wave, we inject a sinusoidal source current \mathbf{J}^f in the form of $J_x^f = J_x^0 \sin(\omega t)$, $i=x,y,z$, where J_x^0 is the amplitude and ω is the angular frequency. Since \mathbf{J}^f only has the x -component, the electric field of the incident THz wave only has E_x component. We set $J_x^0 = 1 \times 10^{11}$ A/m², leading to a peak amplitude of $E_x^{0,\text{inc}} = 18836$ V/m. Under this electric field, the steady-state polarization oscillation is within the harmonic regime even at the resonant condition (see Supplemental Material [30]). Figure 1(c) shows the simulated steady-state evolution of the E_x^{inc} and the resultant ΔP_x at the topmost cell of a 10-nm-thick (100) BaTiO₃ slab at three different angular frequencies ω of the incident THz wave, from which the peak amplitude ΔP_x^0 and phase φ (with respect to the incident wave) can be extracted. During evolution, both the polarization and the THz wave are spatially uniform at such a small thickness (10 nm), thus the simulation results should be consistent with analytical predictions via the formulae derived in Sect. II. Figure 2(a) shows the frequency-dependent $|\Delta P_x^0|$ and φ under three different values of damping coefficient γ . $|\Delta P_x^0|$ is smaller under larger γ due to larger energy dissipation in the lattice of BaTiO₃, and the corresponding φ is shown in the inset. The simulated $|\Delta P_x^0|(\omega)$ and $\varphi(\omega)$ both agree well with those calculated analytically via Eqs. (8a-b). The $|\Delta P_x^0|$ shows a resonant enhancement at $\omega = \omega_x = 2\pi \times 4.1084$ THz when γ is relatively small (2×10^{-7} $\Omega \cdot \text{m}$ and 2×10^{-5} $\Omega \cdot \text{m}$). However, the $|\Delta P_x^0|$ decreases monotonically with increasing ω when γ is relatively large (6×10^{-5} $\Omega \cdot \text{m}$), because the effective damping coefficient $\gamma^{\text{eff}} = \gamma + \frac{1}{2} \frac{d}{k_0 c}$ in this case ($\sim 6.19 \times 10^{-5}$ $\Omega \cdot \text{m}$) is near the threshold ($= 2\omega_x \mu = 6.97 \times 10^{-5}$ $\Omega \cdot \text{m}$) for overdamping (as discussed in Ref. [13]). We also applied the \mathbf{J}^f along the y axis to produce an incident THz electric field of the same peak amplitude along y . The initial equilibrium polarization is still along $+x$. In this case, the numerically simulated ΔP_i is mainly along the y axis (see Supplemental Material [30]). Figure 2(b) shows the $|\Delta P_y^0|(\omega)$ and $\varphi(\omega)$ obtained from both analytical calculations and dynamical phase-field simulations, which are well consistent with each other. Likewise, the $|\Delta P_y^0|$ shows a resonant enhancement at $\omega = \omega_y = 2\pi \times 1.0531$ THz when γ is relatively small (2×10^{-7} $\Omega \cdot \text{m}$) yet decreases monotonically with increasing ω at larger γ . Since the threshold γ^{eff} for overdamping is $\sim 1.79 \times 10^{-5}$ $\Omega \cdot \text{m}$ ($= 2\omega_y \mu$), the polarization oscillation becomes overdamped for the cases of $\gamma = 2 \times 10^{-5}$ $\Omega \cdot \text{m}$ and 6×10^{-5} $\Omega \cdot \text{m}$.

Knowing $|\Delta P_x^0|(\omega)$ and $\varphi(\omega)$ allows evaluating the total electric field at the A_2 plane $E_x^{A_2}(t)$ via Eq. (10), and thus the calculation of the transmission coefficient. Figure 3(a) and 3(b) show the frequency-dependent transmission of the incident THz wave E_x^{inc} and E_y^{inc} under different γ values in a 10-nm-thick film, respectively. The peak amplitude of the source current is $J_i^0 = 1 \times 10^{11}$ A/m² ($i=x,y$). The numerically simulated transmission coefficients agree remarkably well with the analytically calculated values. As shown in both figures, the transmission coefficient is larger at smaller γ value under off-resonance condition ($\omega \ll$

ω_i or $\omega \gg \omega_i$). In this case, the transmission is dominated by the phase difference φ . Take the regime of $\omega \ll \omega_x$ as an example, a smaller γ leads to a larger $|\Delta P_x^0|$ (Fig. 2(b)) and therefore a larger amplitude for the E_x^{rad} . However, the phase difference φ is smaller at smaller γ values (Fig. 2(b) inset). Accordingly, the destructive interference, described by the second term of Eq. (10), is less significant, and thus a larger transmission is achieved. For near ($\omega \sim \omega_i$) or on-resonance ($\omega = \omega_i$) condition, the transmission coefficient is smaller at smaller γ values. In this regime, the phase difference φ is near or equal to $\pi/2$ (see Eq. (8b)). Therefore, the transmission is dominated by the amplitude $|\Delta P_x^0|$. Specifically, the larger $|\Delta P_x^0|$ at smaller γ value leads to a larger amplitude of E_x^{rad} and thus more significant destructive interference. As a result, the transmission coefficient is smaller.

Figure 4(a,d) show both the analytically calculated and numerically simulated thickness-dependent transmission coefficients of the incident THz wave E_x^{inc} and E_y^{inc} at three different frequency values, and Figures 4(b,e) show the zoom-in plot at lower thicknesses. The γ is $2 \times 10^{-7} \Omega \cdot \text{m}$, and the J_i^0 is $1 \times 10^{11} \text{ A/m}^2$ ($i=x,y$) in all cases. As mentioned previously, the analytical model (via Eq. (10)) assumes both the polarization and the THz wave are spatially uniform during evolution, which can only be true when the film thickness d is significantly smaller than THz wavelength in the ferroelectric slab $\lambda_0 = \frac{2\pi}{k^{\text{Re}}}$. Here \mathbf{k}^{Re} is the real part of the complex wavenumber \mathbf{k} of the incident THz wave in the ferroelectric slab, with $\mathbf{k} = \mathbf{k}^{\text{Re}} + i\mathbf{k}^{\text{Im}} = \omega \sqrt{\kappa_0 \kappa_{ii}(\omega) \mu_0}$, where $\kappa_{ii}(\omega)$ is the complex dielectric permittivity whose expression is provided in the text below Eq. (7). The expressions of \mathbf{k}^{Re} and \mathbf{k}^{Im} are provided in Supplemental Material [30]. Assuming that $\kappa_{ii}(\omega)$ in the thick slab is the same as that in the thin slab limit and that $\gamma_i^{\text{eff}} \approx \gamma_i$, we analytically obtain that $\lambda_0 = 7.838 \mu\text{m}$, $0.698 \mu\text{m}$, and $2701.53 \mu\text{m}$ for E_x^{inc} at $2\pi \times 2.6084 \text{ THz}$, $2\pi \times 4.1084 \text{ THz}$ ($=\omega_x$), and $2\pi \times 8.1084 \text{ THz}$, respectively, and $\lambda_0 = 10.550 \mu\text{m}$, $1.379 \mu\text{m}$, and $2536.878 \mu\text{m}$ for E_y^{inc} at $2\pi \times 0.5531 \text{ THz}$, $2\pi \times 1.0531 \text{ THz}$ ($=\omega_y$), and $2\pi \times 5.0531 \text{ THz}$, respectively.

As shown in Figs. 4(a,d) and more clearly in Figs. 4(b,e), while good consistency between analytical and numerical results is reached in the thin slab limit (e.g., $d < 200 \text{ nm}$ for E_x^{inc} at $2\pi \times 4.1084 \text{ THz}$, Fig. 4(b)), significant deviation appears at larger thicknesses. In particular, while the transmission decreases monotonically with increasing thickness for frequencies above the resonant frequency, oscillatory behaviors appear for frequencies below the resonant frequency. Such distinct transmission behaviors are attributed to the stronger attenuation of higher-frequency THz waves and the formation of standing polarization/THz waves in the lower-frequency cases, which we elaborate from the following two aspects. First, by writing the incident THz wave as $E_i^{\text{inc}} = E_i^{0,\text{inc}} e^{i(\mathbf{k}z - \omega t)} = E_i^{0,\text{inc}} e^{-k_i^{\text{Im}} z} e^{-i(k_i^{\text{Re}} z - \omega t)}$ ($i=x,y$), one can see that the imaginary part of the wavenumber \mathbf{k}^{Im} determines the attenuation for the incident wave. Figure 4(c,f) show the analytically calculated frequency dependence of the k_i^{Im} for the E_x^{inc} and E_y^{inc} , respectively. As shown, k_i^{Im} peaks at the resonant frequency ($\omega = \omega_i$), indicating the strongest wave attenuation. Moreover, k_i^{Im} at above ω_i is orders-of-magnitude larger than those below ω_i , indicating a stronger attenuation for higher-frequency THz wave, which is consistent with the monotonic decrease in transmission at $2\pi \times 8.1084 \text{ THz}$ (5.0531 THz) for E_x^{inc} (E_y^{inc}). Second, the relatively low k_i^{Im} at below ω_i suggests that the incident THz wave can propagate across the entire film thickness and interfere with the reflected THz waves. It is this interference that leads to the oscillatory transmission coefficient seen at $2\pi \times 2.6084 \text{ THz}$ (0.5531 THz) for E_x^{inc} (E_y^{inc}). More detailed analyses show that the first, second, and third peaks in the oscillatory transmission curve correspond to the formation of $n=1, 2, 3$ mode standing THz wave (i.e., $\frac{n\pi}{d} = k^{\text{Re}}$), respectively (see Supplemental Material [30]). This phenomenon can be explained

by approximately writing the standing THz wave to be $E_i^{\text{stand}} \approx Ae^{-k^{\text{Im}}z}e^{-i(k^{\text{Re}}z-\omega t)} + Be^{-k^{\text{Im}}(2d-z)}e^{-i(-k^{\text{Re}}z-\omega t)}$ with $0 \leq z \leq d$, from which it can be seen that E_i^{stand} peaks when $z = \frac{n\pi}{k^{\text{Re}}}$.

V. Conclusions

We have developed an LGD-theory based analytical model for predicting the frequency- and thickness-dependent THz wave transmission across ferroelectrics at the thin slab limit in the regime of steady-state harmonic excitation. The analytical model indicates that the polarization-current-induced radiation electric field increases the effective damping coefficient for polarization dynamics. A larger effective damping reduces the amplitude of polarization excitation, leading to a higher THz wave transmission, yet in the meantime modulates the phase difference between the polarization oscillation and the incident electric field that results in lower THz wave transmission. Which mechanism dominates the transmission depends on whether the THz wave frequency is near or off resonance with the ferroelectric polarization. When the ferroelectric slab thickness is significantly smaller than the THz wavelength inside the ferroelectrics, the predictions from the analytical model agree well with simulation results from a dynamical phase-field model, which incorporates coupled dynamics of polarization, strain, and EM waves in multiphase systems. The excellent consistence demonstrates that both approaches are valid. At large thicknesses, the transmission behavior is governed by the propagation, attenuation, and reflection of THz wave inside the ferroelectric as well as the resulting formation of standing polarization/THz waves, which is revealed by our dynamical phase-field simulations.

The strong absorption at or near the resonant frequency suggests the potential of realizing an effective electric-field control of the THz wave transmission through the modulation of the spontaneous polarization at the initial equilibrium and the resultant resonant frequency. Our analytical model can be used to analyze experimentally measured steady-state THz wave transmission spectra in single-domain ferroelectrics in the harmonic regime and thin slab limit, which allow extracting key parameters such as the mass and damping coefficients of polarization dynamics and probe the local curvature of the free energy landscape. The analytical model can be readily extended to include the influence of temperature and epitaxial strain, which modifies the landscape of the Landau energy. The dynamical phase-field model permits simulating THz transmission in more general cases including large-amplitude THz excitation and systems with inhomogeneous polarization configuration such as polar vortices [42] and skyrmions [43]. The dynamical phase-field model can be used to design the polarization domain structure of single-phase ferroelectrics or ferroelectric heterostructures (e.g., multilayer, superlattices) for realizing on-demand control over the propagation, transmission, and reflection of THz wave for high-data-rate wireless communication. Both the analytical theory and dynamical phase-field models can be generalized to investigate THz wave transmission for other polar materials that have spontaneous polarization and piezoelectric effect such as III-nitride semiconductors.

Acknowledgement

The work at University of Wisconsin-Madison was supported by the National Science Foundation (NSF) under the grant number DMR-2237884. The effort at Penn State is supported by the NSF through Grant No. DMR- 2133373. Part of this work was performed under the auspices of the U.S. Department of Energy by Lawrence Livermore National Laboratory under Contract DE-AC52-07NA27344 (B.W.). The dynamical phase-field simulations were performed using Bridges at the Pittsburgh Supercomputing Center through allocation TG-DMR180076 from the Advanced Cyberinfrastructure Coordination Ecosystem: Services & Support (ACCESS) program, which is supported by NSF grants #2138259, #2138286, #2138307, #2137603, and #2138296.

References

- [1] H.-J. Song and N. Lee, *Terahertz Communications: Challenges in the Next Decade*, IEEE Trans. Terahertz Sci. Technol. **12**, 105 (2022).
- [2] A. Leitenstorfer, A. S. Moskalenko, T. Kampfrath, J. Kono, E. Castro-Camus, K. Peng, N. Qureshi, D. Turchinovich, K. Tanaka, A. G. Markelz, M. Havenith, C. Hough, H. J. Joyce, W. J. Padilla, B. Zhou, K.-Y. Kim, X.-C. Zhang, P. U. Jepsen, S. Dhillon, M. Vitiello, E. Linfield, A. G. Davies, M. C. Hoffmann, R. Lewis, M. Tonouchi, P. Klarskov, T. S. Seifert, Y. A. Gerasimenko, D. Mihailovic, R. Huber, J. L. Boland, O. Mitrofanov, P. Dean, B. N. Ellison, P. G. Huggard, S. P. Rea, C. Walker, D. T. Leisawitz, J. R. Gao, C. Li, Q. Chen, G. Valušis, V. P. Wallace, E. Pickwell-MacPherson, X. Shang, J. Hesler, N. Ridler, C. C. Renaud, I. Kallfass, T. Nagatsuma, J. A. Zeitler, D. Arnone, M. B. Johnston, and J. Cunningham, *The 2023 Terahertz Science and Technology Roadmap*, J. Phys. D. Appl. Phys. **56**, 223001 (2023).
- [3] H.-T. Chen, W. J. Padilla, J. M. O. Zide, A. C. Gossard, A. J. Taylor, and R. D. Averitt, *Active Terahertz Metamaterial Devices*, Nature **444**, 597 (2006).
- [4] H.-T. Chen, S. Palit, T. Tyler, C. M. Bingham, J. M. O. Zide, J. F. O'Hara, D. R. Smith, A. C. Gossard, R. D. Averitt, W. J. Padilla, N. M. Jokerst, and A. J. Taylor, *Hybrid Metamaterials Enable Fast Electrical Modulation of Freely Propagating Terahertz Waves*, Appl. Phys. Lett. **93**, 91117 (2008).
- [5] C. W. Berry, J. Moore, and M. Jarrahi, *Design of Reconfigurable Metallic Slits for Terahertz Beam Modulation*, Opt. Express **19**, 1236 (2011).
- [6] T. Kleine-Ostmann, P. Dawson, K. Pierz, G. Hein, and M. Koch, *Room-Temperature Operation of an Electrically Driven Terahertz Modulator*, Appl. Phys. Lett. **84**, 3555 (2004).
- [7] T. Kleine-Ostmann, K. Pierz, G. Hein, P. Dawson, M. Marso, and M. Koch, *Spatially Resolved Measurements of Depletion Properties of Large Gate Two-Dimensional Electron Gas Semiconductor Terahertz Modulators*, J. Appl. Phys. **105**, 93707 (2009).
- [8] B. Sensale-Rodriguez, R. Yan, M. M. Kelly, T. Fang, K. Tahy, W. S. Hwang, D. Jena, L. Liu, and H. G. Xing, *Broadband Graphene Terahertz Modulators Enabled by Intraband Transitions*, Nat. Commun. **3**, 780 (2012).
- [9] H.-T. Chen, W. J. Padilla, M. J. Cich, A. K. Azad, R. D. Averitt, and A. J. Taylor, *A Metamaterial Solid-State Terahertz Phase Modulator*, Nat. Photonics **3**, 148 (2009).
- [10] Z. Miao, Q. Wu, X. Li, Q. He, K. Ding, Z. An, Y. Zhang, and L. Zhou, *Widely Tunable Terahertz Phase Modulation with Gate-Controlled Graphene Metasurfaces*, Phys. Rev. X **5**, 41027 (2015).
- [11] Z. Chen, X. Chen, L. Tao, K. Chen, M. Long, X. Liu, K. Yan, R. I. Stantchev, E. Pickwell-MacPherson, and J.-B. Xu, *Graphene Controlled Brewster Angle Device for Ultra Broadband Terahertz Modulation*, Nat. Commun. **9**, 4909 (2018).
- [12] J. Petzelt and S. Kamba, *Far Infrared and Terahertz Spectroscopy of Ferroelectric Soft Modes in Thin Films: A Review*, Ferroelectrics **503**, 19 (2016).
- [13] S. Zhuang and J.-M. Hu, *Role of Polarization-Photon Coupling in Ultrafast Terahertz Excitation of Ferroelectrics*, Phys. Rev. B **106**, L140302 (2022).
- [14] P. Kužel and F. Kadlec, *Tunable Structures and Modulators for THz Light*, Comptes Rendus Phys. **9**, 197 (2008).

- [15] C. Kadlec, V. Skoromets, F. Kadlec, H. Němec, J. Hlinka, J. Schubert, G. Panaitov, and P. Kužel, *Temperature and Electric Field Tuning of the Ferroelectric Soft Mode in a Strained SrTiO₃/DyScO₃ Heterostructure*, Phys. Rev. B - Condens. Matter Mater. Phys. **80**, 174116 (2009).
- [16] C. Kadlec, F. Kadlec, H. Němec, P. Kužel, J. Schubert, and G. Panaitov, *High Tunability of the Soft Mode in Strained SrTiO₃/DyScO₃ Multilayers*, J. Phys. Condens. Matter **21**, 115902 (2009).
- [17] P. Kužel, C. Kadlec, F. Kadlec, J. Schubert, and G. Panaitov, *Field-Induced Soft Mode Hardening in SrTiO₃/DyScO₃ Multilayers*, Appl. Phys. Lett. **93**, 52910 (2008).
- [18] J. Hlinka, T. Ostapchuk, D. Nuzhnyy, J. Petzelt, P. Kuzel, C. Kadlec, P. Vanek, I. Ponomareva, and L. Bellaiche, *Coexistence of the Phonon and Relaxation Soft Modes in the Terahertz Dielectric Response of Tetragonal BaTiO₃*, Phys. Rev. Lett. **101**, 167402 (2008).
- [19] R. Jiang, Z. Han, W. Sun, X. Du, Z. Wu, and H.-S. Jung, *Ferroelectric Modulation of Terahertz Waves with Graphene/Ultrathin-Si:HfO₂/Si Structures*, Appl. Phys. Lett. **107**, 151105 (2015).
- [20] J. Ji, S. Zhou, J. Zhang, F. Ling, and J. Yao, *Electrical Terahertz Modulator Based on Photo-Excited Ferroelectric Superlattice*, Sci. Rep. **8**, 2682 (2018).
- [21] I. Katayama, H. Aoki, J. Takeda, H. Shimosato, M. Ashida, R. Kinjo, I. Kawayama, M. Tonouchi, M. Nagai, and K. Tanaka, *Ferroelectric Soft Mode in a SrTiO₃ Thin Film Impulsively Driven to the Anharmonic Regime Using Intense Picosecond Terahertz Pulses*, Phys. Rev. Lett. **108**, 97401 (2012).
- [22] S. Grübel, J. A. Johnson, P. Beaud, C. Dornes, A. Ferrer, V. Håborets, L. Huber, T. Huber, A. Kohutych, and T. Kubacka, *Ultrafast X-Ray Diffraction of a Ferroelectric Soft Mode Driven by Broadband Terahertz Pulses*, ArXiv Prepr. ArXiv1602.05435 (2016).
- [23] F. Chen, Y. Zhu, S. Liu, Y. Qi, H. Y. Hwang, N. C. Brandt, J. Lu, F. Quirin, H. Enquist, P. Zalden, T. Hu, J. Goodfellow, M.-J. Sher, M. C. Hoffmann, D. Zhu, H. Lemke, J. Glowina, M. Chollet, A. R. Damodaran, J. Park, Z. Cai, I. W. Jung, M. J. Highland, D. A. Walko, J. W. Freeland, P. G. Evans, A. Vailionis, J. Larsson, K. A. Nelson, A. M. Rappe, K. Sokolowski-Tinten, L. W. Martin, H. Wen, and A. M. Lindenberg, *Ultrafast Terahertz-Field-Driven Ionic Response in Ferroelectric BaTiO₃*, Phys. Rev. B **94**, 180104 (2016).
- [24] Q. Li, V. A. Stoica, M. Paściak, Y. Zhu, Y. Yuan, T. Yang, M. R. McCarter, S. Das, A. K. Yadav, S. Park, C. Dai, H. J. Lee, Y. Ahn, S. D. Marks, S. Yu, C. Kadlec, T. Sato, M. C. Hoffmann, M. Chollet, M. E. Kozina, S. Nelson, D. Zhu, D. A. Walko, A. M. Lindenberg, P. G. Evans, L.-Q. Chen, R. Ramesh, L. W. Martin, V. Gopalan, J. W. Freeland, J. Hlinka, and H. Wen, *Subterahertz Collective Dynamics of Polar Vortices*, Nature **592**, 376 (2021).
- [25] T. Qi, Y.-H. Shin, K.-L. Yeh, K. A. Nelson, and A. M. Rappe, *Collective Coherent Control: Synchronization of Polarization in Ferroelectric PbTiO₃ by Shaped THz Fields*, Phys. Rev. Lett. **102**, 247603 (2009).
- [26] Q. Zhang, R. Herchig, and I. Ponomareva, *Nanodynamics of Ferroelectric Ultrathin Films*, Phys. Rev. Lett. **107**, 177601 (2011).
- [27] R. Herchig, K. Schultz, K. McCash, and I. Ponomareva, *Terahertz Sensing Using Ferroelectric Nanowires*, Nanotechnology **24**, 45501 (2013).
- [28] S. Prosandeev, J. Grollier, D. Talbayev, B. Dkhil, and L. Bellaiche, *Ultrafast Neuromorphic Dynamics Using Hidden Phases in the Prototype of Relaxor Ferroelectrics*, Phys. Rev. Lett. **126**, 27602 (2021).

- [29] G. D. Landry and T. A. Maldonado, *Zigzag Analysis of Interference Effects in an Arbitrarily Oriented Biaxial Single Layer*, J. Opt. Soc. Am. A **13**, 1737 (1996).
- [30] See *Supplemental Material* at [URL] for Derivations of the polarization-current-induced radiation electric field and the coefficients A_i and B_i in the expression of resonant frequencies; control calculations on the electromagnetic wave transmission across a dielectric with $\mathbf{P}=0$; harmonic fitting of the Landau energy landscape; the full temporal evolution profile of ΔP_i ($i=x,y$) under resonant excitation by E_y^{inc} ; spatial profiles of the standing polarization/THz wave.
- [31] T. Yang and L.-Q. Chen, *Dynamical Phase-Field Model of Coupled Electronic and Structural Processes*, Npj Comput. Mater. **8**, 130 (2022).
- [32] T. Yang, B. Wang, J.-M. Hu, and L.-Q. Chen, *Domain Dynamics under Ultrafast Electric-Field Pulses*, Phys. Rev. Lett. **124**, 107601 (2020).
- [33] Vitalii L Ginzburg, *Phase Transitions in Ferroelectrics: Some Historical Remarks*, Physics-Uspokhi **44**, 1037 (2001).
- [34] P. Tang, R. Iguchi, K. Uchida, and G. E. W. Bauer, *Excitations of the Ferroelectric Order*, Phys. Rev. B **106**, L081105 (2022).
- [35] A. Widom, S. Sivasubramanian, C. Vittoria, S. Yoon, and Y. N. Srivastava, *Resonance Damping in Ferromagnets and Ferroelectrics*, Phys. Rev. B **81**, 212402 (2010).
- [36] D. C. Ma, Y. Zheng, and C. H. Woo, *Phase-Field Simulation of Domain Structure for $\text{PbTiO}_3/\text{SrTiO}_3$ Superlattices*, Acta Mater. **57**, 4736 (2009).
- [37] A. K. Tagantsev, *The Role of the Background Dielectric Susceptibility in Uniaxial Ferroelectrics*, Ferroelectrics **69**, 321 (1986).
- [38] A. P. Levanyuk, B. A. Strukov, and A. Cano, *Background Dielectric Permittivity: Material Constant or Fitting Parameter?*, Ferroelectrics **503**, 94 (2016).
- [39] A. N. Morozovska, Y. M. Vysochanskii, O. V Varennyk, M. V Silibin, S. V Kalinin, and E. A. Eliseev, *Flexocoupling Impact on the Generalized Susceptibility and Soft Phonon Modes in the Ordered Phase of Ferroics*, Phys. Rev. B **92**, 94308 (2015).
- [40] J. J. Wang, X. Q. Ma, Q. Li, J. Britson, and L.-Q. Chen, *Phase Transitions and Domain Structures of Ferroelectric Nanoparticles: Phase Field Model Incorporating Strong Elastic and Dielectric Inhomogeneity*, Acta Mater. **61**, 7591 (2013).
- [41] R. Zu, B. Wang, J. He, L. Weber, A. Saha, L.-Q. Chen, and V. Gopalan, *Optical Second Harmonic Generation in Anisotropic Multilayers with Complete Multireflection Analysis of Linear and Nonlinear Waves Using# SHAARP. Ml Package*, ArXiv Prepr. ArXiv2307.01368 (2023).
- [42] A. K. Yadav, C. T. Nelson, S. L. Hsu, Z. Hong, J. D. Clarkson, C. M. Schlepütz, A. R. Damodaran, P. Shafer, E. Arenholz, L. R. Dedon, D. Chen, A. Vishwanath, A. M. Minor, L. Q. Chen, J. F. Scott, L. W. Martin, and R. Ramesh, *Observation of Polar Vortices in Oxide Superlattices*, Nature **530**, 198 (2016).
- [43] S. Das, Y. L. Tang, Z. Hong, M. A. P. Gonçalves, M. R. McCarter, C. Klewe, K. X. Nguyen, F. Gómez-Ortiz, P. Shafer, E. Arenholz, V. A. Stoica, S.-L. Hsu, B. Wang, C. Ophus, J. F. Liu, C. T. Nelson, S. Saremi, B. Prasad, A. B. Mei, D. G. Schlom, J. Íñiguez, P. García-Fernández, D. A. Muller, L. Q. Chen, J. Junquera, L. W. Martin, and R. Ramesh, *Observation of Room-Temperature Polar Skyrmions*, Nature **568**, 368 (2019).

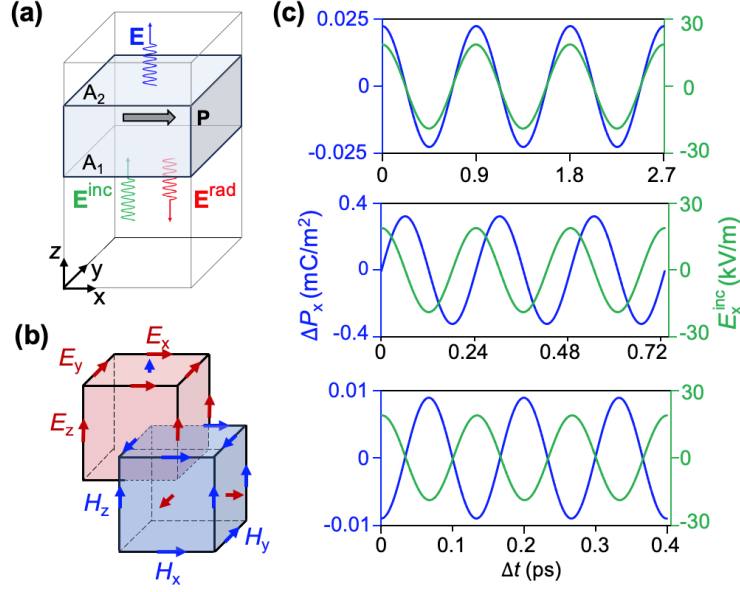


Figure 1. (a) Schematic of the system set-up for studying THz wave transmission across a freestanding ferroelectric layer with a single-domain spontaneous polarization \mathbf{P} at the initial equilibrium state. The incident THz wave (\mathbf{E}^{inc}) is produced by a free charge current source \mathbf{J}^{f} . The electric-field component of the transmitted THz wave \mathbf{E} is a superposition of the \mathbf{E}^{inc} and the polarization-current ($\partial\mathbf{P}/\partial t$) induced radiation electric field \mathbf{E}^{rad} . The reflected THz wave is \mathbf{E}^{rad} . (b) Schematic of the Yee lattice where staggered cells are used for discretization of the \mathbf{E} and \mathbf{H} component of the THz wave in our dynamical phase-field model. (c) Numerically simulated steady-state evolution of the E_x^{inc} and the resultant ΔP_x at the topmost cell of a 10-nm-thick (100) BaTiO₃ slab. (From top to bottom) the angular frequency of E_x^{inc} $\omega=2\pi\times 1.1084$ THz, $2\pi\times 4.1084$ THz ($=\omega_x$, on-resonance), and $2\pi\times 7.5084$ THz, respectively.

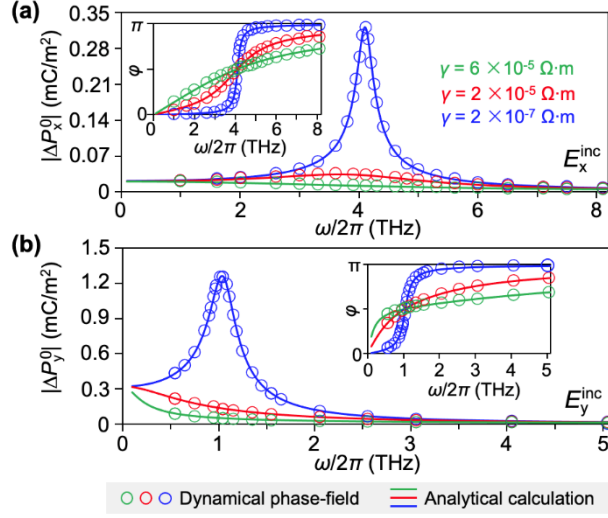


Figure 2. Amplitude $|\Delta P_i^0|$ and phase φ (inset) of the steady-state harmonic polarization oscillation $\Delta P_i(t) = \Delta P_i^0 e^{i(-\omega t + \varphi)}$ in a 10-nm-thick (100) BaTiO₃ slab under the excitation of E_i^{inc} of different angular frequency ω with different damping coefficient γ , with the subscript $i=x$ for (a) and $i=y$ for (b).

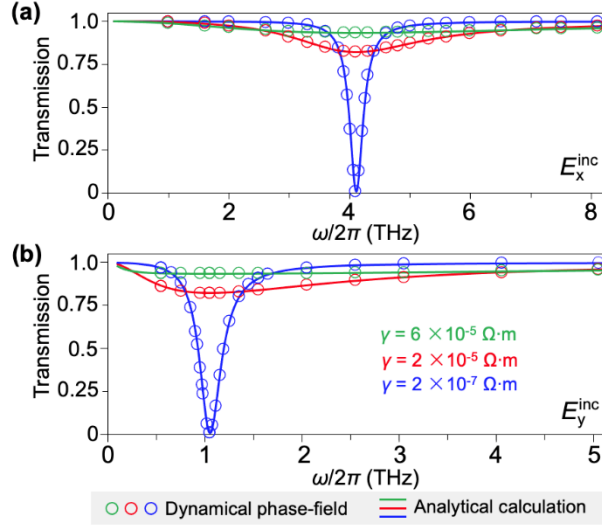


Figure 3. Frequency-dependent transmission of (a) E_x^{inc} and (b) E_y^{inc} THz wave across a 10-nm-thick (100) BaTiO₃ slab under different damping coefficient γ .

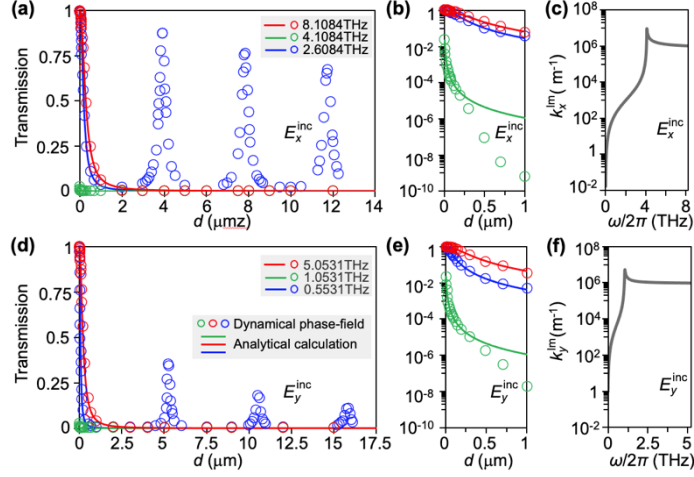


Figure 4. Thickness-dependent transmission coefficients for (a) E_x^{inc} and (c) E_y^{inc} across a (100) BaTiO₃ slab under a fixed damping coefficient $\gamma=2\times 10^{-7} \Omega\cdot\text{m}$ at three different frequencies, obtained by analytical calculation (solid lines) and dynamical phase-field simulations (symbols). (b,e) Their zoom-in figures at low thicknesses, with log-scale transmission coefficients. Frequency-dependent imaginary part of the complex wavenumber for (c) E_x^{inc} and (f) E_y^{inc} , respectively, obtained by analytical calculations.